


Article

Finite Element Modelling of a Parabolic Trough Collector for Concentrated Solar Power

Andrea Gilioli ¹, Francesco Cadini ^{1,*}, Luca Abbiati ¹, Giulio Angelo Guido Solero ², Massimo Fossati ¹, Andrea Manes ¹ , Lino Carnelli ³, Carla Lazzari ³, Stefano Cardamone ³ and Marco Giglio ¹

¹ Dipartimento di Meccanica—Politecnico di Milano, via La Masa 1, 20156 Milan, Italy; andrea.gilioli@polimi.it (A.G.); lucavincenzoabbiati@mail.polimi.it (L.A.); massimo.fossati@polimi.it (M.F.); andrea.manes@polimi.it (A.M.); marco.giglio@polimi.it (M.G.)

² Dipartimento di Energia—Politecnico di Milano, via Lambruschini, 20156 Milan, Italy; giulio.solero@polimi.it

³ ENI SpA, Renewable Energy & Environmental R&D Center, Istituto ENI Donegani, 28100 Novara, Italy; lino.carnelli@eni.it (L.C.); Carla.Lazzari@eni.it (C.L.); Stefano.Cardamone@eni.it (S.C.)

* Correspondence: francesco.cadini@polimi.it; Tel.: +39-2-23996355

Abstract: Nowadays the design of large-scale structures can be effectively improved by the adoption of numerical models. Even if experimental tests still play a fundamental role, a methodological approach that combines experimental testing and modelling technique can significantly improve the understanding of the matter. This, in fact, would result in a more reliable optimization process, drastically reducing efforts and uncertainties towards the implementation of the final product. The present work deals with the development of a finite element model for the analysis of a full-scale prototype of an innovative parabolic trough collector. The collector is analysed under several load conditions in order to evaluate its structural behaviour. Each load configuration is also numerically reproduced. Moreover, it is demonstrated that the model is capable of reproducing both the global (stiffness) and local (strain state) behaviour of the structure. Specifically, the comparison between experimental data and numerical results show a good agreement for the global parameter torsional stiffness. Local strain values are also well reproduced in high-stressed zone. Thus, the model can be used as a reliable “virtual tool” for designers to evaluate the suitability of layout modifications, thereby replacing and reducing the amount of commonly needed experimental tests and, consequently, reducing time and costs. Finally, an example of the potentiality of the finite element model adopted for a computer-aided engineering approach is shown to determine the most promising solution for increasing the torsional stiffness of the trough, while simultaneously limiting the required experimental tests.

Keywords: solar energy; concentrated solar power system; parabolic trough collector; numerical model; FEM; structural integrity



Citation: Gilioli, A.; Cadini, F.; Abbiati, L.; Solero, G.A.G.; Fossati, M.; Manes, A.; Carnelli, L.; Lazzari, C.; Cardamone, S.; Giglio, M. et al. Finite Element Modelling of a Parabolic Trough Collector for Concentrated Solar Power. *Energies* **2021**, *14*, 209. <https://doi.org/10.3390/en14010209>

Received: 16 November 2020

Accepted: 29 December 2020

Published: 3 January 2021

Publisher’s Note: MDPI stays neutral with regard to jurisdictional claims in published maps and institutional affiliations.



Copyright: © 2021 by the authors. Licensee MDPI, Basel, Switzerland. This article is an open access article distributed under the terms and conditions of the Creative Commons Attribution (CC BY) license (<https://creativecommons.org/licenses/by/4.0/>).

1. Introduction

Concentrated solar power systems (CSP) are an attractive solution for the production of green energy. Therefore, companies and researchers have progressively put more efforts into the investigation of the potentialities of this technology, [1]. CSP production systems are based on mirrors which reflect the sunlight onto a receiver, in which a transfer fluid flows that is heated up by solar energy. By exploiting this working scheme, the produced heat can be expended directly for end-use applications, or for the generation of green electricity through conventional steam turbines and other applications [2]. Because of its importance, the receiver is a complex component, whose thermal performances have been, for example, studied in [3]. Even though the intuition at the base of the CSP was attributed to Archimedes (212 B.C.) [4], in 2014, only approximately 5 gigawatts worldwide were installed by means of this technology. The main reason for the still not widespread adoption of CSPs lies in their yet not fully competitive energy production costs, which are still higher compared to other energy production methods, as also reported in References [5,6]. More

specifically, according to [7,8], a large margin of possible cost reduction is related to the improvement of the construction of the solar fields and the collectors themselves. This result can be achieved by means of an optimized design, leading to a reduction of the optical error and to an increase of the lifetime of the field. In case of structural investigations, as in the present research work, finite element methods (FEM) represent efficient analysis tools, as previously reported in References [9,10]. In References [11,12] the FE modelling approach is mainly exploited to investigate the mirror shape. Also, in References [13] finite element analysis (FEA) has been used to assess the trough collector design considering gravity, temperature gradients and wind loads. Once the FE models are validated, i.e., the numerical results are compared with the data obtained from a limited number of experimental tests showing good accuracy, it is reasonable to apply the same model to investigate new and unknown (not tested experimentally) load cases and geometry variations. This approach is also known as computer aided design (CAD), because it represents a design procedure aided by the adoption of many numerical simulations. The advantages are evident and mainly consist of a reduction of costs and time related to the reduced number of experimental tests.

The present research work thus focuses on:

- The development of a numerical model of an innovative parabolic trough collector, initially devised at the Massachusetts Institute of Technology (MIT) (US20170082322, Low cost parabolic cylindrical trough for concentrated solar power) and developed by ENI in collaboration with Politecnico di Milano and MIT;
- The assessment of its accuracy to reproduce both its local and global behaviour by means of comparisons with experimental tests described in [11].

As far as the authors know, no other works in the literature describe the modelling of an entire large parabolic trough at the detail level proposed in the present paper and with the large amount of data obtained from the measurements during the tests. Here, the same model is adopted for both global (stiffness level) and local (local strain) assessments. Moreover, the parabolic trough has been designed and built exploiting the large use of an adhesive layer, together with more standard bolted joint. This made the design quite innovative with respect to the actual ones.

2. Numerical Model of the Parabolic Trough Collector

Note that, for brevity's sake, the detailed description of the trough prototype and of the experimental activity carried out at the laboratories of the Politecnico di Milano to test its performances are reported in the paper [14] by some of the same authors of the present work. The interested reader is kindly referred to that paper and to the further works [15–21] for a thorough overview of the prototype and of the novel technological solutions distinguishing its design from those available on the market. Specifically, in the references [18,19] the novelty aspect of the design of the present parabolic trough collector are discussed in detail. The main material used for the building of the parabolic trough has qualities similar to DD11 steel.

The model was generated exploiting the commercial software Pre/Post ABAQUS CAE 2016 and the results were computed using the STANDARD ABAQUS solver. Each simulation was run on an 8 Cores/16 Threads Intel XEON 5630@4Ghz CPU with 64 Gb of RAM memory. The computational time depends on the adopted mesh size and, for the analyses developed in the current research, the range was from 1 h up to a maximum of 96 h. The duration appears very reasonable for such a complex model and the adopted workstation is a good system, even though its performance is very far from a system with a specific server with hundreds of CPUs. The starting input for the development of the FE model (Figure 1b) is a 3D CAD drawing made using the Autodesk Inventor software, representing all the components of the structure (Figure 1a). The geometry of the parabolic trough is composed mainly of thin components and therefore the structural parts were modelled by means of shell elements (S4R). This solution was adopted since a solid model of the whole parabolic trough collector requires an extremely high number of elements and

hence it results in a non-feasible requirement of memory and CPU computational time. Additionally, the use of solid elements for thin walled structures (like in the present case) is not only computationally inefficient but it could also lead to inaccurate results in terms of reproduction the stress\strain state. Vice versa, 2D shell elements are very efficient for such investigations. Moreover, some specific components, with one geometrical dimension much longer than the others, were modelled using the 1D beam element. Example of these components are the bolts and the receiver supports. The aim of the model is to provide a global insight into the mechanical behaviour of the trough and, thus it is more important to correctly model a realistic stiffness of the joints/supports than to model a very detailed state of stress resulting in a drastic increase in computational costs. More specific, assessment on joint may be carried out using sub-modelling technique that replicates the joints with higher accuracy. However, this technique requires dedicated efforts and it is out of the scope of the present paper. For instance, the beam elements, even if the local stress\strain state is approximated, allow for an effective analysis of the internal forces and moments in order to compute further assessment. Finally, it is worth remembering that only linear elements, with a reduced integration scheme, have been adopted. Nonlinear analysis considering the large displacement has been developed too; however, considering the applied loads\displacements, the result is only an increase of calculation time without any significant improvement of result accuracy. Finally, thermal stresses have not been considered in the present analyses.

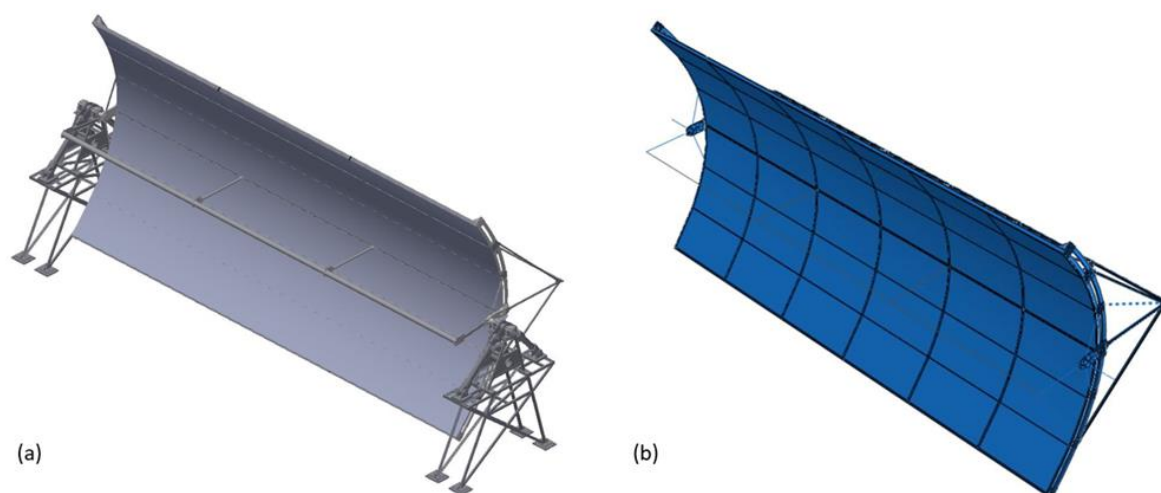


Figure 1. (a) Computer aided design (CAD) model. (b) Finite element model.

In total four different static load cases, and therefore four different numerical models, were developed (each model differs from the others only for the applied loads and boundaries). The choice of the loads cases is aimed to test the parabolic trough collector in critical conditions even more dangerous than the real working ones, replicating the load applied during the experimental activities described in [14] and, as reported previously, studying the limit deformation which guarantees to retain a reasonable optical efficiency. In order to evaluate the effect of the mesh on the results, all models were developed using two different mesh sizes, one coarse and the other very refined (Figure 2). Indeed, the parabolic trough collector represents a very large full-scale system and an adequate balance between the accuracy of the results and the calculation time and memory required is, therefore, difficult to achieve. Common models are developed using a coarse mesh in order to get global results regarding the overall behaviour of the structure and sub models are developed with a refined mesh in order to get a very detailed view of the local stress\strain field. The adoption of sub models is not always straightforward as a proper communication between the global and local model needs to be guaranteed and this often leads to some discrepancies and inaccuracies. In the present simulations, no sub modelling technique

has been adopted and thus a very refined mesh is necessary to simultaneously determine the local (stress\strain field) and global behaviour (stiffness) of the structure. However, refinement of the mesh was carried out on the same geometrical model. The advantage of this approach is a higher accuracy of the results, but the drawback are the high numerical resources requested (up to 50 Gb memory with up to 96 h calculation time). Therefore, two different mesh levels have been considered to determine the extent to which the mesh affects both the local and global behaviour of the structure.

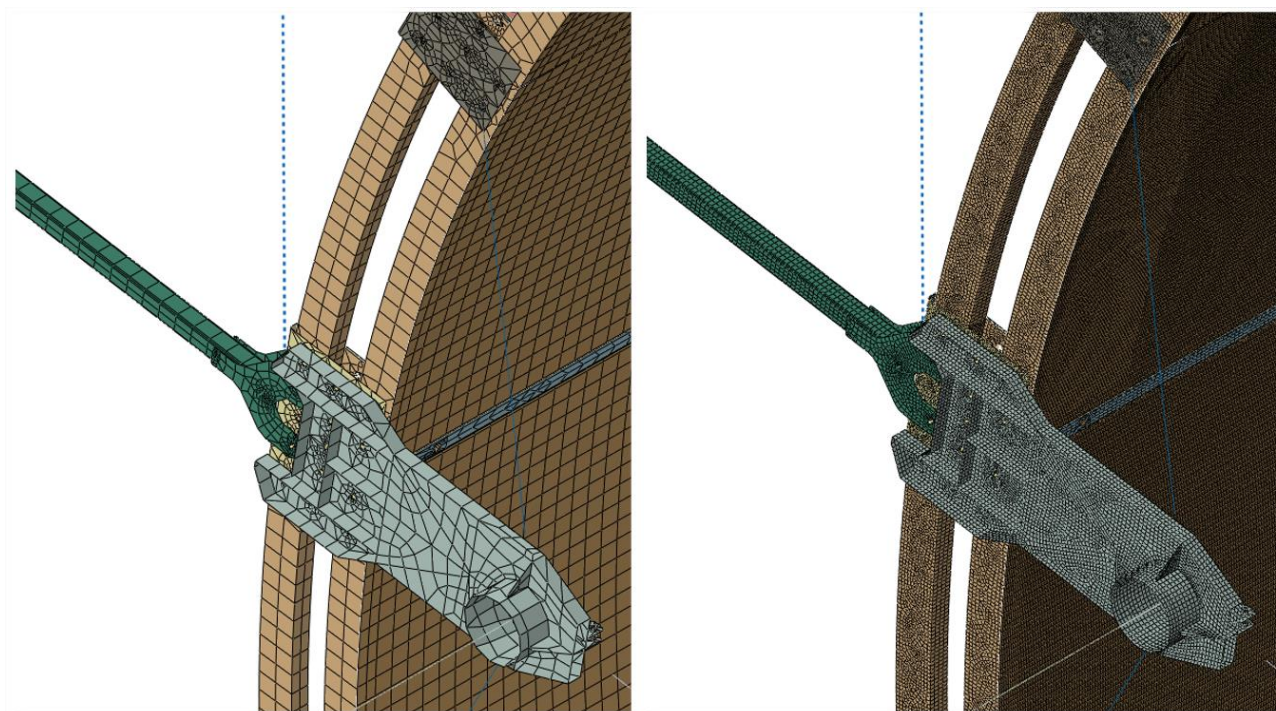


Figure 2. Examples of different mesh sizes: coarse on the left, refined on the right.

Hence, in the next sections, the models are described according to the sequence of the actions with which they have been built.

2.1. Part and Assembly

All of the parts have been created by converting the 3D solid geometry used in the CAD model to a shell geometry. Some discrepancies between the real solid model and the shell model must be taken into account, but a conservative approach has been taken for all the assumptions and approximations in order to modify the starting model as little as possible. The modifications have been made to improve the calculation performances without affecting the results. A list of the principal components of the structure is reported below:

- The ribs (Figure 3a)
- The joints (Figure 3b)
- The panel (Figure 3c)
- The king post (Figure 3d)

All of the parts previously listed are then placed in the correct position creating the assembly of the system, in accordance with the CAD model. In Figure 4, the model of the entire parabolic trough collector is shown.

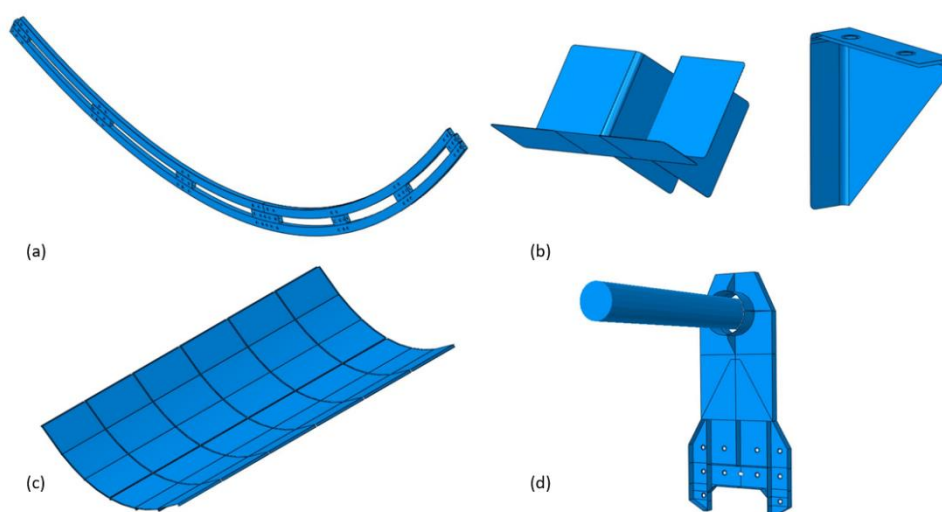


Figure 3. Numerical model of the most important parts of the trough: (a) end rib, (b) internal joints, (c) panel assembly, (d) king post.

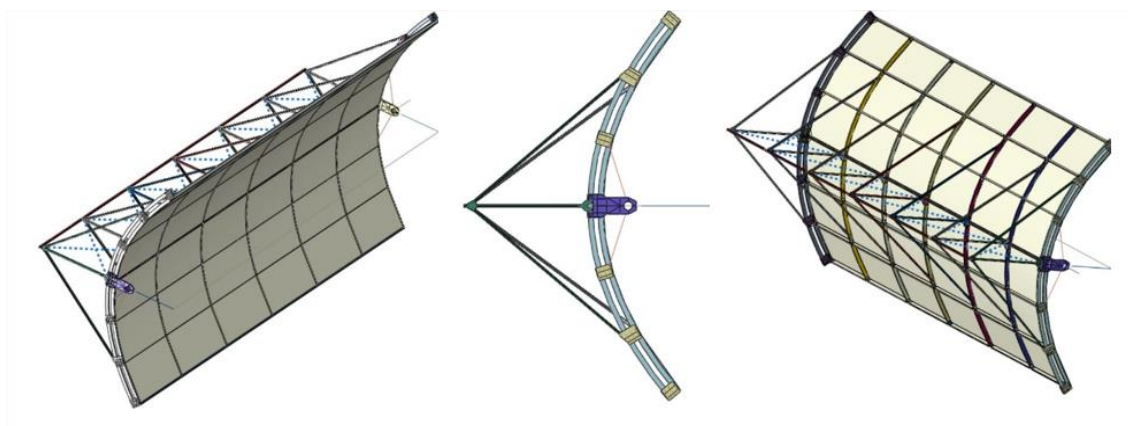


Figure 4. Assembly preview.

2.2. Interaction

It is worth pointing out that the mere placement of each component in the correct position is not sufficient to define their reciprocal interaction. There are three kinds of connections in the models and each interaction has its specific behaviour, that can be exploited to properly reproduce the real connection between the parts:

- **Couplings:** surface-based coupling constraint that provides coupling between a reference node and a group of nodes referred to as the ‘coupling nodes’. In the present case, this type of constraint creates a connection between a point on a beam, called master node, and the nodes on the border of the hole, called slave nodes: thereby the group of nodes is constrained to the rigid body motion of a single node, Figure 5a.
- **Tie:** a tie constraint ties two separate surfaces together abolishing any relative motion between them. In particular, it constrains the displacements of the nodes of one surface to move synchronically with the nodes of another surface. It can be considered as an infinitely rigid, zero thickness glue connection, Figure 5b.
- **Connectors:** special couplings that can link the degrees of freedom of two nodes and assign a behaviour (such as the structural stiffness) to that connection for each coupled degree. In the current case, they have been used to model the back-tie rods, made of steel wire, which can be also regulated in the axial direction in order to obtain the desired preload, Figure 5c.

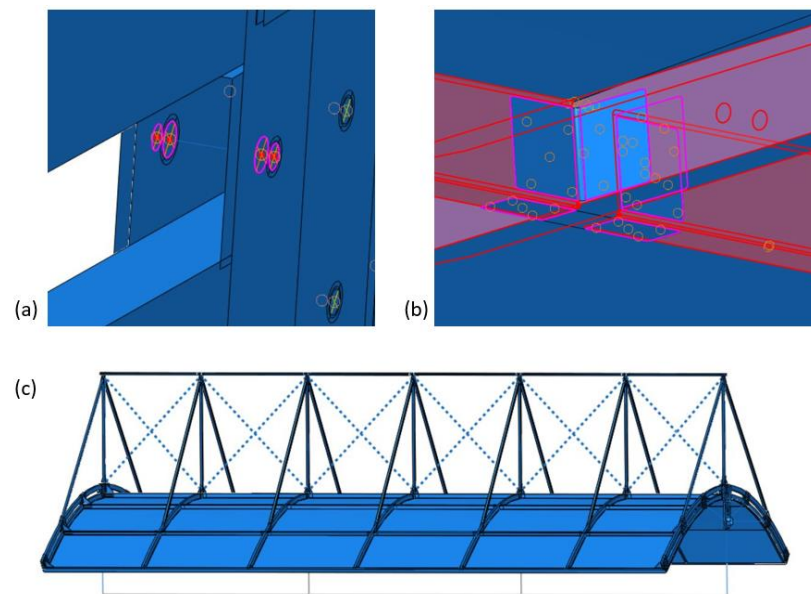


Figure 5. (a) Coupling pairing, (b) tie constraint between adhesive layer and the joint, (c) connectors reproducing the back-crossing tie rods.

2.3. Load and Boundaries

In this section, the general loads and the boundary conditions applied to the models are described. Indeed, the specific loads applied to replicate each experimental test are described in detail in the Sections 3.1–3.4. The general load and boundaries introduced here are the gravity load and the boundary conditions related to the constraints with respect to the ground. The gravitational load was imposed for the whole model, defining an acceleration field equal to 9.81 m/s^2 directed as the negative y-axis (Figure 6a).

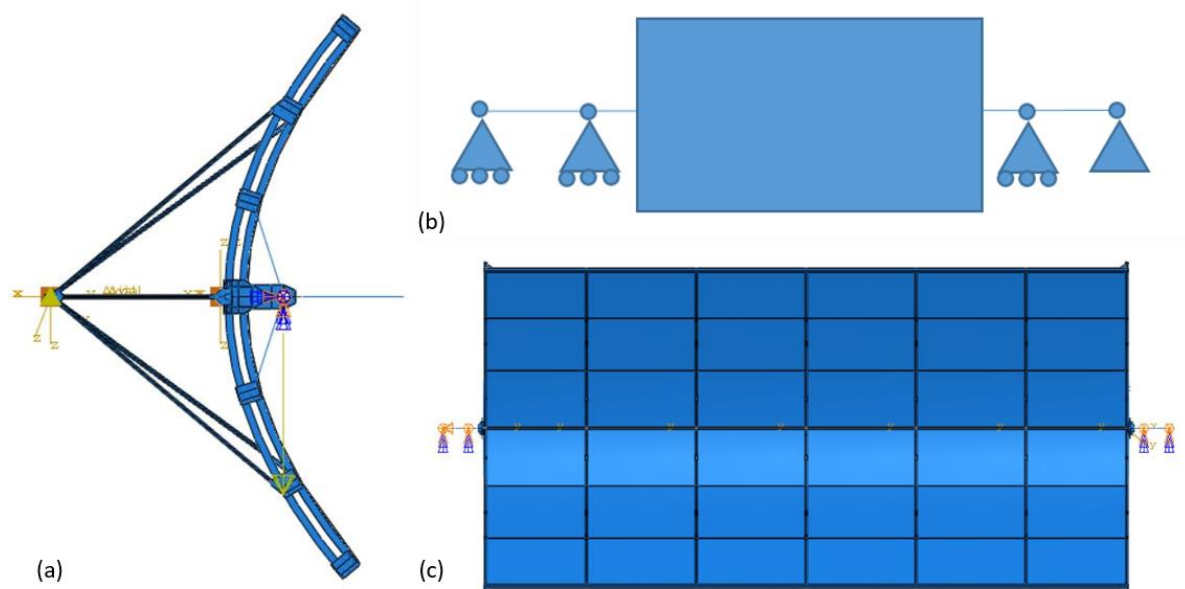


Figure 6. (a) Gravitational load, (b) bearing scheme, (c) bearing representation in the finite element (FE) model.

The real prototype of the parabolic trough collector is constrained to the ground by means of two bearings for each side, placed on two reticular bases. In the present model, three bearings have been considered as sliders and the last one as a hinge, therefore only one of the bearings blocks the axial translation, which, on the other hand, is allowed by

the other three bearings. A scheme of the bearings is shown in Figure 6b, while Figure 6c shows the model highlighting the points used to represent the bearings.

2.4. Mesh

The definition of the mesh for each part of the model requires a preliminary partition of the surfaces in order to allow, where possible, a sweep or a structured meshing technique aimed at a more regular and homogeneous discretization. This is of particular importance because it can guarantee more efficient numerical solving. A global seed with dimensions from 4 mm to 10 mm is assigned to the various parts. Moreover, in localized areas of particular interest such as the holes or the adhesive layers, a smaller local seed is assigned (Figure 7). For the most refined model, a total number of about 4.8 million elements have been used, while a total number of about 180,000 elements have been used for the coarse model. The data related to the elements used are shown in the Tables 1 and 2. Depending on the nature of the part, different types of elements have been used:

- Solid elements C3D8R
- Shell elements S4R
- Beam elements B31

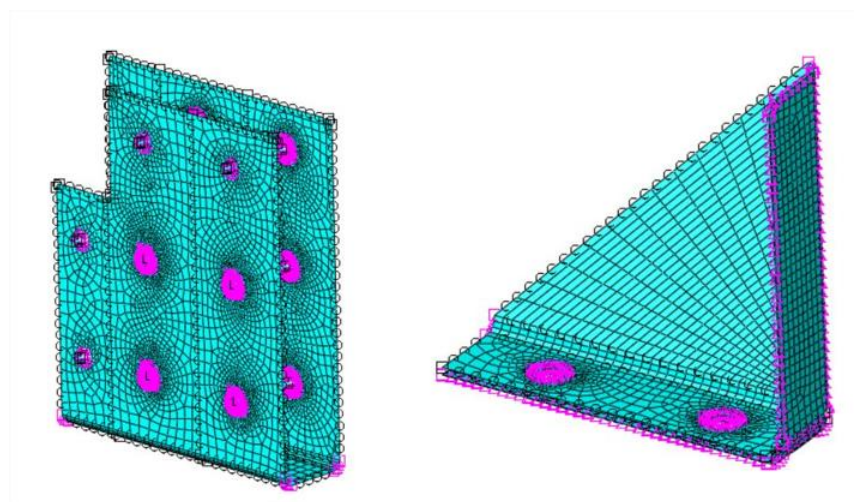


Figure 7. Examples of part seeding.

Table 1. Mesh statistics for the coarse model.

Total Number of Nodes		186,945		
Total number of elements		178,282		
Element type				
S4R	Quadrilateral	Linear	152,722	
S3	Triangular	Linear	11,787	
C3D8R	Hexahedral	Linear	9454	
B31	Beam	Linear	4319	

Table 2. Mesh statistics for the refined model.

Total Number of Nodes		4,841,985		
Total number of elements		4,879,343		
Element type				
S4R	Quadrilateral	Linear	4,058,061	
S3	Triangular	Linear	19,600	
C3D8R	Hexahedral	Linear	796,480	
B31	Beam	Linear	5202	

Only linear elements have been adopted with a reduced integration scheme in order to reduce the calculation time while maintaining good accuracy.

3. Case Studies

In this section, the case studies adopted to assess the structural behaviour of the collector under several loads are reported. In particular for each test the load and the boundary conditions adopted in the model, and the validation process of the numerical model, which compares the experimental and the numerical results, are briefly described. In the present activity, the validation has been performed on two levels: globally and locally. The global validation is based on the comparison of the torsional stiffness and the displacement measured by lasers and cables sensors placed in relevant points [14]. The local validation is performed by comparing the local strain with the measure obtained experimentally by the strain gauges' sensors. In more detail, the local validation consists of the comparison of the numerical strain state with the experimental measurements obtained by means of a series of strain gauges placed on several relevant points of the trough (see [14]). The choice of the position of the sensor network is based in order to acquire significant strain values for all the experimental configurations tested. Hence, for each configuration, not all the strain gauges provide relevant values. Depending on the load case, some of the gauges measure high strain values, while others are almost unloaded as expected. Because of the physical sensibility of the strain gauges and owing to the entire measurement chain, very low values are not relevant (the noise overcomes the physical signal; thus, they are of no interest for the comparison). Therefore, for each load case only the most relevant strain gauges have been compared. It is very important to remark also the fact that, in the FE model, the results are not continuous everywhere, but the structure is discrete with the elements as a base unit. Hence, results are averaged on the dimension of the element and some possible discrepancies can arise when compared with the experiment. Another source of possible variability is caused by the position of the strain gauges. In fact, even if all the locations of the strain gauges are measured, some minor differences between the FE model and experiments potentially remains. Additionally, if a strain gauge is placed in a location with a high stress (strain) gradient, the comparisons become complex leading to potentially larger differences.

3.1. Differential Torsion Test

The differential torsion represents one of the most important loads which is applied on the parabolic trough because it is similar to a real working condition when the system has to be moved in the presence of wind and is driven by the torsional stiffness that is a peculiar feature of this system. The torsional stiffness is of primary importance for a parabolic trough because it is closely related to the behaviour of the structure during a working cycle and this means that in order to design the manoeuvring system it is important to know the stiffness behaviour of the trough. Moreover, the efficiency of the system can be profoundly affected by its stiffness behaviour. The FE model replicates the experimental test, hence the rotation of one end of the trough is fixed whilst on the other a rotation is imposed. During the experimental test, the torque and the rotational angle are measured. In the real system rotation is applied by actuators at one side when on the other side the actuators act in order to avoid any rotation. The rotation is acquired by means of an encoder and the torque by means of torsional strain gauges. At the same time, two lasers measure the horizontal displacement of the trough respectively at the middle and at one end of the bottom traverse [14]. Also, two cable sensors are applied at the two top ends of the trough to measure such a displacement. With regards to the loads, they are applied in the models in two different steps: at first the gravity (the weight of the structure) and then, in the second step, the rotation of one end of the trough is applied. It is worth to summarize graphically the kind of constraint applied to the system, as shown in Figure 8.

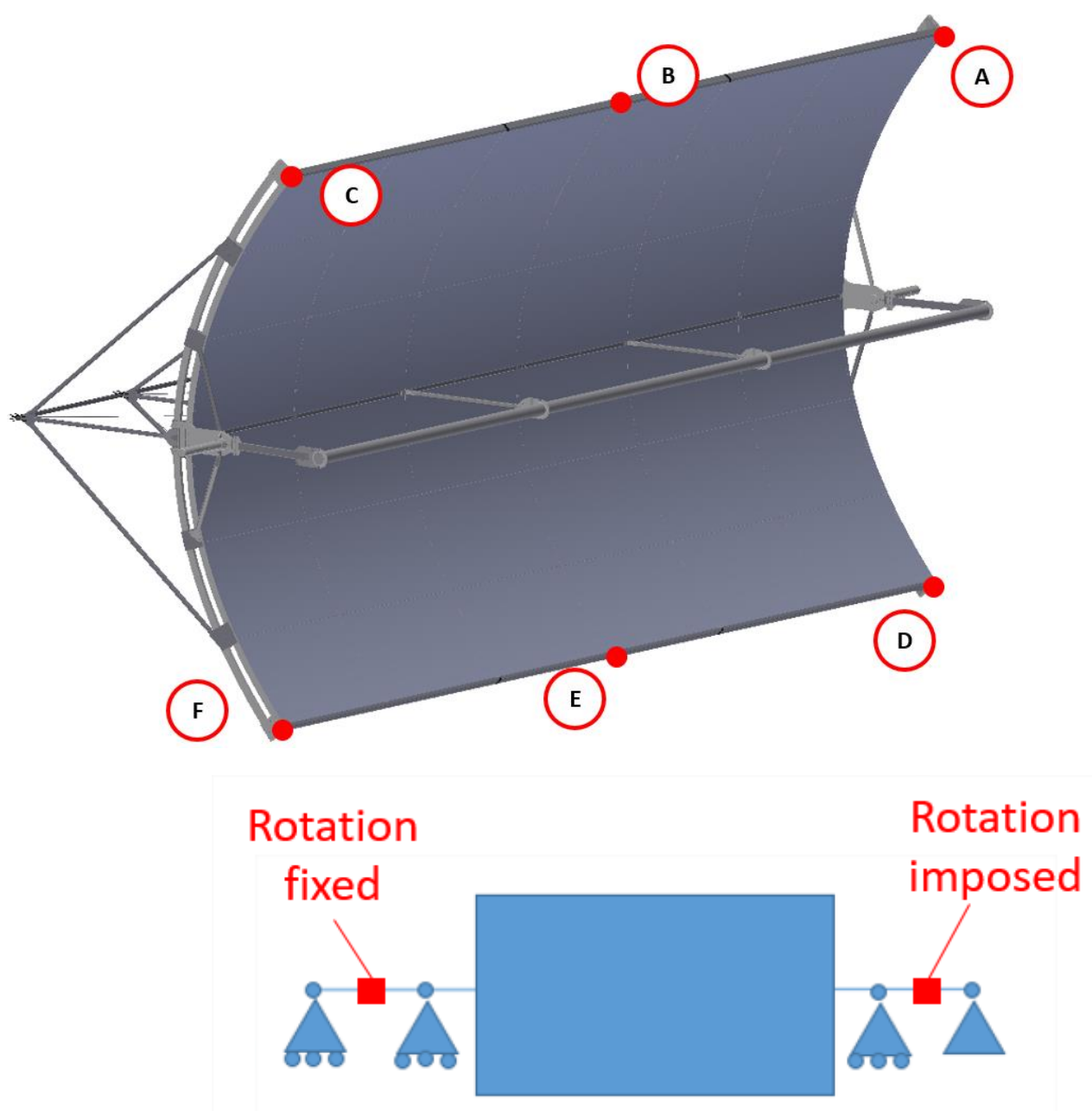


Figure 8. Sensor position is depicted in the upper figure whereas boundaries applied in the differential torsion model are reported in the lower figure.

In order to reproduce the real configuration of the actuators, a midpoint between the constraints (that replicate the bearings has been created) and a rotation is imposed on it.

The global validation consists of the comparisons (experimental data with numerical results) of the torsional stiffness, the displacement of the cables and the lasers. Because of the fact that the parabolic trough collector is an actual industrial prototype, specific data about the torsional stiffness cannot be provided. Therefore, data in some of the following Figures and Tables will be provided upon removal the actual scale and actual values. However, the comparison between experimental data and numerical results will be reported in detail with the actual value of the errors.

The comparisons are done not only describing the displacement as a function of the rotation angle but also as a function of the torque (moment) applied to the shaft of the trough.

The comparison of the torsional stiffness of the trough between the experiments and the FE model is shown in Figure 9. It is important to remember that in the experimental set-up the torque is measured on both sides of the trough by means of a couple of strain gauges placed on the two shafts to connect it to the supports. Theoretically the torque read on both sides has to be equal due to the symmetry of the problem however the values are slightly different. These differences are part of the natural experimental variation of the test and the quantification of the estimated error of the torsional stiffness is reported in Table 3.

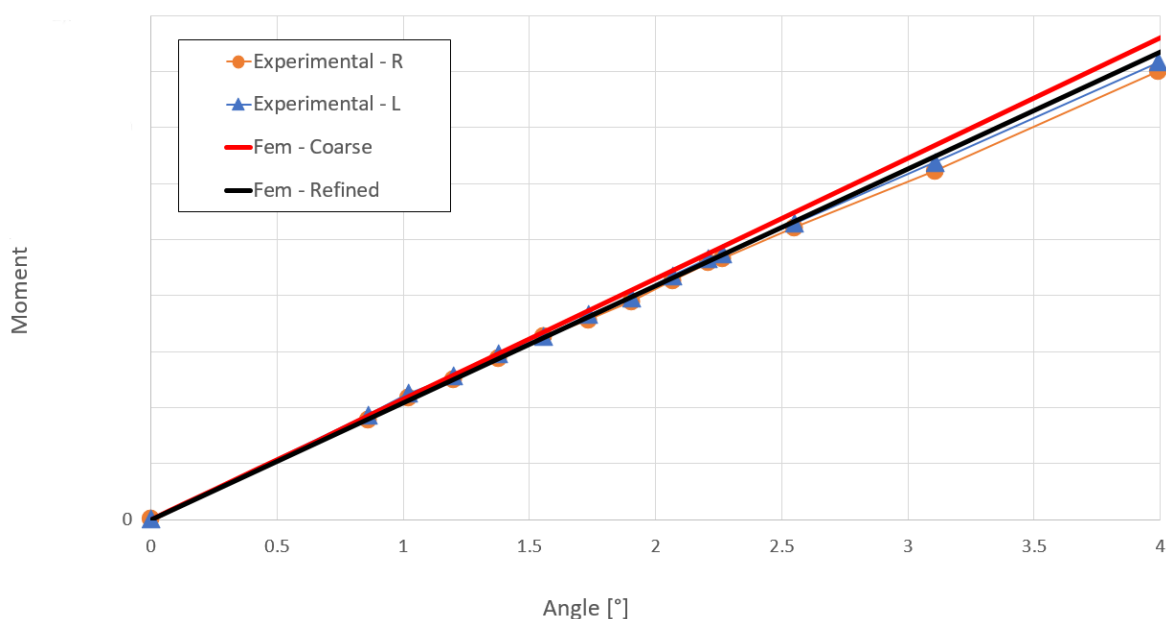


Figure 9. Comparison between the FE moment-angle curve and the corresponding experimental curve obtained considering the torque measure on the right shaft (R) and the left shaft (L) for the differential torsion test.

Table 3. Comparison of the errors between experimental and numerical torsional stiffness values for the two FE models (finer and coarser).

Side	FE Refined Stiffness	FE Coarse Stiffness
	Error (%)	Error (%)
Left	2.77	5.69
Right	4.49	7.25

The maximum error of the refined model is around 4% when considering the torque applied on the right shaft and only around 2% when considering the left side. However, in the coarse model the error increases up to 7%. Considering the complexity of the model, the error values are low, and the numerical estimation of the stiffness is reliable, so that the model can be considered to be validated. Other global comparisons performed regard the displacements measured by the lasers and by the cable transducers. Since the torsional stiffness estimation appears to be very accurate, then also the abovementioned comparisons are expected to be accurate.

Figure 10a,b show the comparison between the experimental measure of the displacement at the laser position (position E and F, see Figure 8) and the corresponding FE values in terms of displacement versus angle (Figure 10a) and displacement versus moment (Figure 10b). The numerical model accurately reproduces the on-field values, both with the refined and coarse models. Some discrepancies are potentially due to the way in which the displacement has been measured experimentally. Indeed, the laser measures not directly on the trough, but on a special measurement support adequately linked to the traverse. Some minor misalignments present can lead to some small apparent discrepancy when

comparing numerical and experimental results. In Figure 10c,d, the comparisons between the displacement measured by cable transducer (Position A and C, see Figure 8) and the numerical model as a function of the rotation angle and as a function of the moment applied on the right shaft are shown. Exactly as for the laser, the FE models replicate with a good accuracy the experimental displacement. In conclusion, the global validation of the FE model for the differential torsion is assessed and the ability of the FE model to reproduce with high reliability and accuracy the experiments is demonstrated.

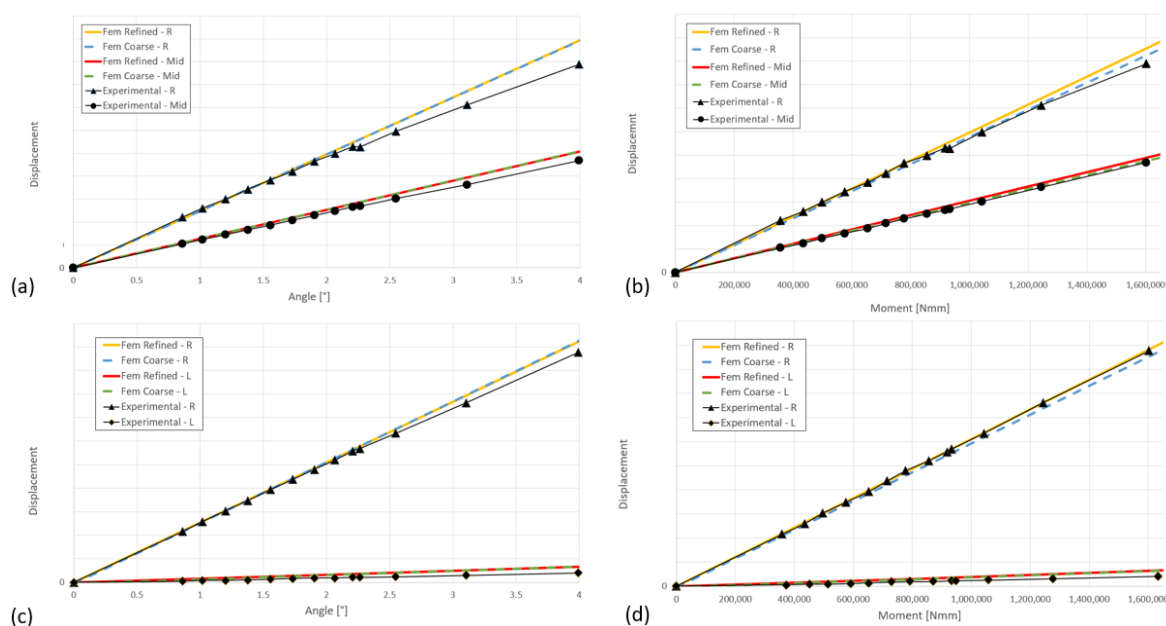


Figure 10. Comparison between experimental and FE displacement for the differential torsion: (a) measured at laser position, as a function of the rotation angle, (b) measured at laser position, as a function of the moment applied on the right side, (c) measured at cable position, as a function of the rotation angle, (d) measured at cable position, as a function of the moment applied on the right side.

Following the demonstration that the FE model is able to accurately reproduce the torsional stiffness and the displacement in various relevant measurement points of the trough, a local assessment validation has been also performed and the results for the most significative strain gauges and the corresponding numerical values are reported in Table 4. At the local scale, some discrepancies can be observed, due to the modelling assumptions, such as, for example, that no temperature gradients effect are taken into account.

Table 4. Comparison between the experimental strain at the maximum torque along with numerical strain evaluated in the differential torsion test for a selected list of strain gauges.

Ext. n.	Experimental $\mu\epsilon$	Numerical $\mu\epsilon$
15	43	25.7
16	9	4
17	−43	−25.7
18	−46	−25.7
19	45	25.7
30	45	30.3
32	−51	−62

3.2. Distributed Bending Test

In order to perform the distributed bending test, a contrast structure has been designed and built. The test consists of rotating the trough on both ends by the same angle, whilst

the contrast structure blocks the movement of the bottom traverse. The bending is defined as distributed because the contrast structure is in contact with the trough for a length of 4 m. As previously done for the differential torsion model, also in this case the reference model has been modified in order to replicate the specific case under examination. The most important difference of the distributed bending model is the introduction of the contrast structure. This structure consists of HE 160B steel beams. In the FE model, the contrast structure has been modelled by means of shell elements for the part in contact with the trough and with beam elements for the vertical supports grounded. In Figure 11a, the model of the contrast structure is reported, while Figure 11b shows the whole model in the distributed bending configuration.

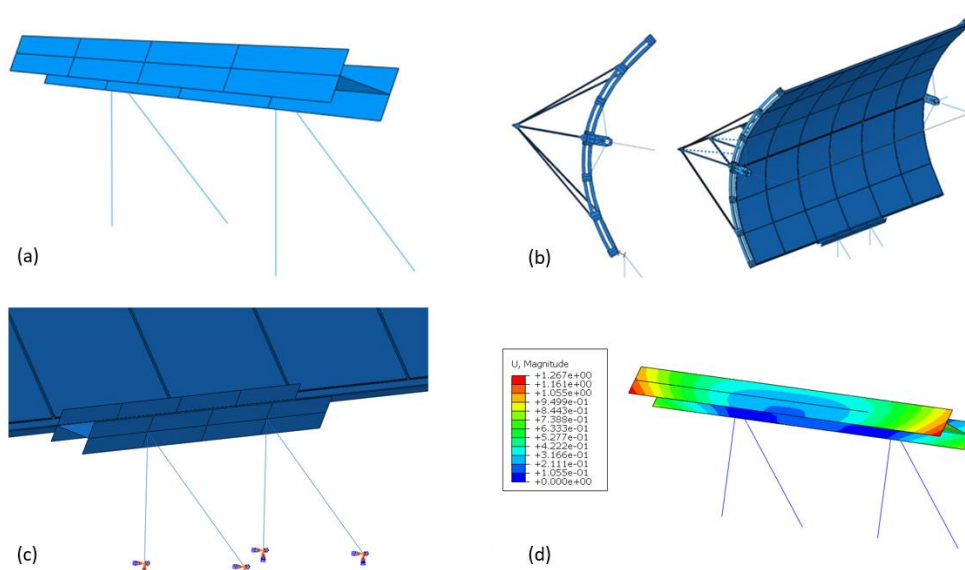


Figure 11. (a) Contrast structure, (b) distributed bending configuration, (c) encastre applied on the contrast structure, (d) contours (in mm) of the displacement magnitude of the contrast structure when the maximum load is applied.

The constraint scheme adopted for this configuration is reported in Figure 12a. As for the torsion, the rotation has been applied in a midpoint between the constraints related to the bearings but in this case this rotation is applied on both ends of the trough while the rotation has been fixed at one end in the differential torsion.

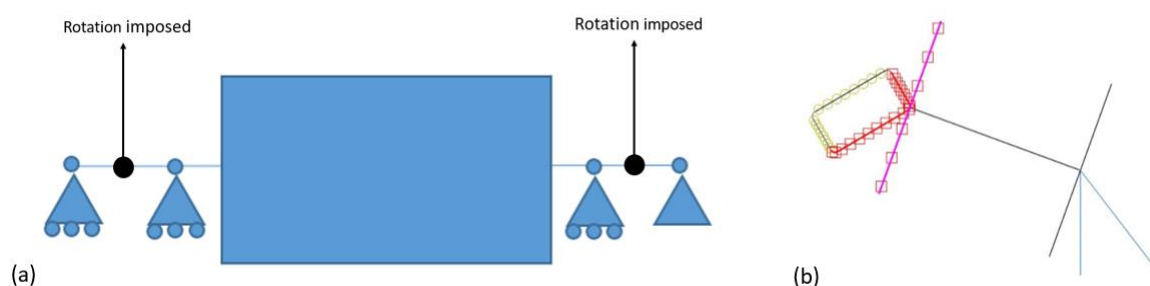


Figure 12. (a) Boundary conditions applied in the distributed bending, (b) contact interaction.

Moreover, the contrast structure has been grounded by four encastres placed at the end of the beam parts, see Figure 11c. The evaluation of the deformation of the contrast structure is required in order to evaluate its stiffness and Figure 11d shows the contours of the displacement magnitude corresponding at the maximum load. In order to model the interaction between the service structure and the traverse, a surface-to-surface contact formulation has been used which defines the surfaces that are involved in this interaction, while also considering the possible sliding between them. In Figure 12b, the surfaces

involved in the contact interaction are highlighted. The contact interaction works fine, and the deformation is realistic and reasonable. In particular, the maximum displacement is of only 1.2 mm which represents a very small value. Hence it is possible to consider the contrast structure almost rigid. Figure 12b shows the surfaces involved in the contact interaction.

The displacement measured by the lasers and by the cable transducers have been compared with the numerical results and the displacements have been evaluated at both the bottom ends of the trough with laser measurements. The central point (Mid position) has not been measured because of the presence of the contrast structure and therefore the area was characterized by very small displacement. Figure 13a,b reports the comparisons of the displacements measured by the lasers, placed at the two bottom ends of the trough and Figure 13a shows a peculiar change in the slope at an angle of 0.1° in the numerical curves. The motivation of this change is purely numerical because in the very first part of the analysis, the software has to solve the problem of the contact between the trough and the contrast structure. Once this issue is numerically solved, the data become very similar to the experimental ones, especially with regards to the slope. Figure 13b, showing the displacements as a function of the applied moment, provides a clear comparison. Again, the FE model is evidently slightly stiffer than the experiments because the displacements are smaller with the same applied moment. Also, the slope of the numerical curves is similar compared to the experimental results and the refined mesh model predictions are slightly better.

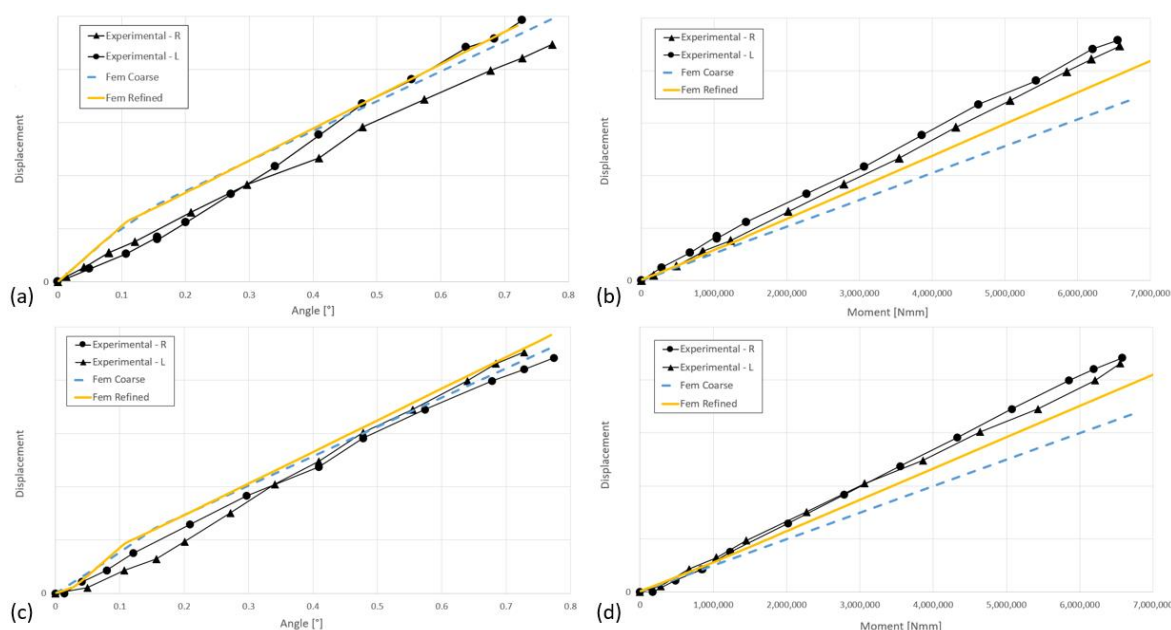


Figure 13. Comparison between experimental and FE displacement in the distributed bending: (a) Measured at laser position, as a function of the rotation angle; (b) measured at laser position, as a function of the moment; (c) measured at cable position, as a function of the rotation angle; (d) measured at cable position, as a function of the moment.

Conclusions similar to the ones obtained for the lasers can be drawn also for the cable transducers, as shown in Figure 13c,d. Again, if the data are plotted as a function of the rotation angle, the results are less clear (Figure 13c) but when data are shown as a function of the applied moment (Figure 13d) the match of the data improves. The global validation of the model of the trough is thus successfully carried on for the distributed bending test. Minor differences can be ascribed to the clearances present in the real trough, which cannot be simulated numerically.

Concerning the local validation, Table 5 reports the measurements of the maximum strain along with other interesting measurements of SG which can help the interpretation

of the strain state in the structure. The numerical strain results are extremely similar compared with the experimental results and the level of accuracy is even higher than for the differential torsion. The accuracy is due to the distributed bending load scenario, which leads, for the points where SG are placed, to a stress gradient lower than the case of the differential torsion and, as already explained above; this allows a better comparison. Not only are the numerical results similar to the experiments, but, upon close inspection, the same symmetry and distribution as the experimental results becomes apparent. Indeed, the distributed bending is a symmetric problem and if the experiment and the numerical model are properly defined, the strain distribution has to be symmetric as well. Therefore, based on the discussion above, also the local validation of the model is thus achieved for the distributed bending test.

Table 5. Comparison between the experimental strain at the maximum load with the numerical strain for the distributed bending evaluated for a selected list of strain gauges.

Ext. n.	Experimental $\mu\epsilon$	Numerical $\mu\epsilon$
1	−122	−111.7
3	−309	−256.1
5	−110	−111.7
16	74	69.9

3.3. Concentrated Bending Test

The concentrated and the distributed bending are similar, apart from one significant difference: only a 160 mm contact surface between the contrast structure and the trough has been adopted instead of the 4 m used for the distributed bending test. Indeed, the contrast structure used for the distributed bending has been modified by considering only one ground support and by replacing the long horizontal beam with a smaller one. The chosen contact zone has been placed in correspondence of the second row of the ribs. As for the differential torsion and the distributed bending, also in this case the reference model has been modified in order to replicate the specific case under examination. The numerical model results are very similar to the distributed bending results as in Figure 14a. The boundaries applied for the concentrated bending have been imposed to replicate the real experimental conditions as well as possible, while the contrast structure, it has been grounded by an encastre similar to the distributed bending set-up, as shown in Figure 14b. The deformation of the contrast structure has been analysed in order to evaluate its stiffness and similarly to the distributed bending. The displacements are small (maximum 0.9 mm), as shown in Figure 14c, and the contrast structure can thus be considered as almost rigid. The contact interaction has been modelled following the identical approach used for the distributed bending. The contact formulation is surface-to-surface and the contact has been considered frictionless. Moreover, it has been imposed that after a surface (or segment) begins to be involved in a contact, the surface has to remain in contact.

The comparison between the laser displacement of the right side of the trough (where the nominal rotation is applied) is reported in two different ways: in Figure 15a, the displacement is reported as a function of the angle, while later it will be reported also as a function of the applied moment. Again, the FE model appears to be stiffer than the experiments and the refined model is always slightly more precise than the coarse model. The apparent discrepancies are not related to the slope of the curve which appears to be always very similar to the experiments, but rather to some local ‘offset’. This is clearly visible at an angle of 0.3° in Figure 15a and at around 500,000 and 4,000,000 N/mm in Figure 15b. Non-linear free plays cannot be completely avoided during the construction of the system, but, on the other hand, they cannot be reproduced by a numerical model so that they are the main reason of these discrepancies. Similar conclusions arise also from the evaluation of the displacements measured by the cable transducer on the right end of the trough. In this case small differences in the accuracy between the coarse and the refined

mesh are present. The numerical slope of the curves shown in Figure 15c,d are very similar to the experimental value.

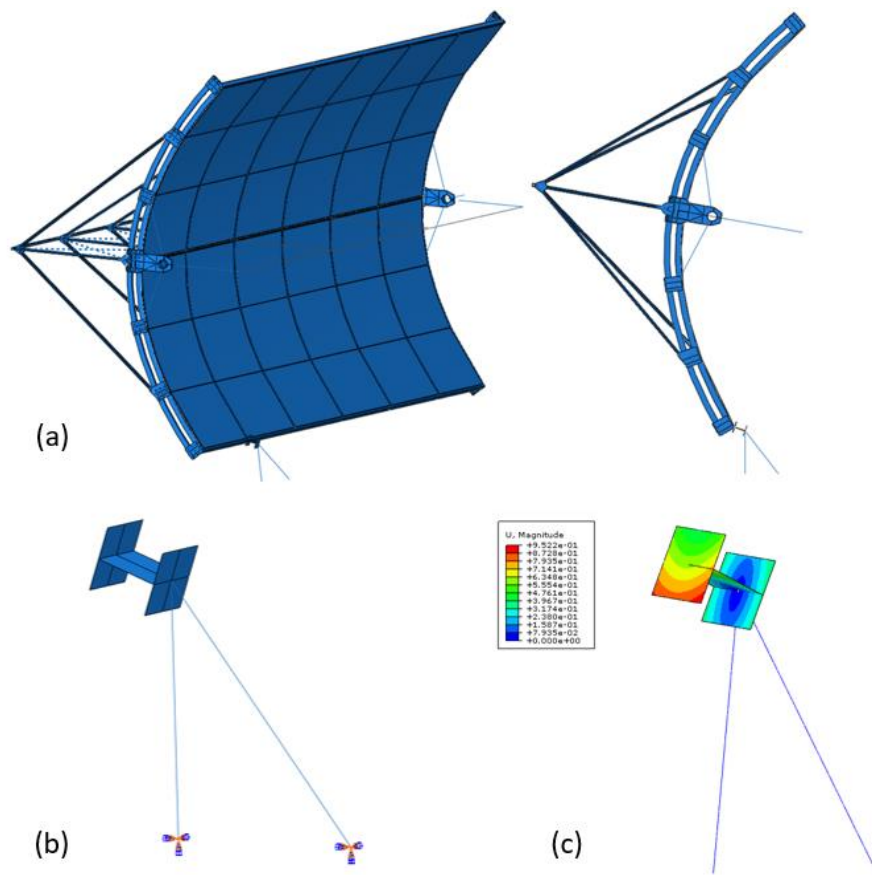


Figure 14. (a) Numerical model of the concentrated bending; (b) encastre applied on the contrast structure; (c) contours of the displacement magnitude of the contrast structure when the maximum load is applied.

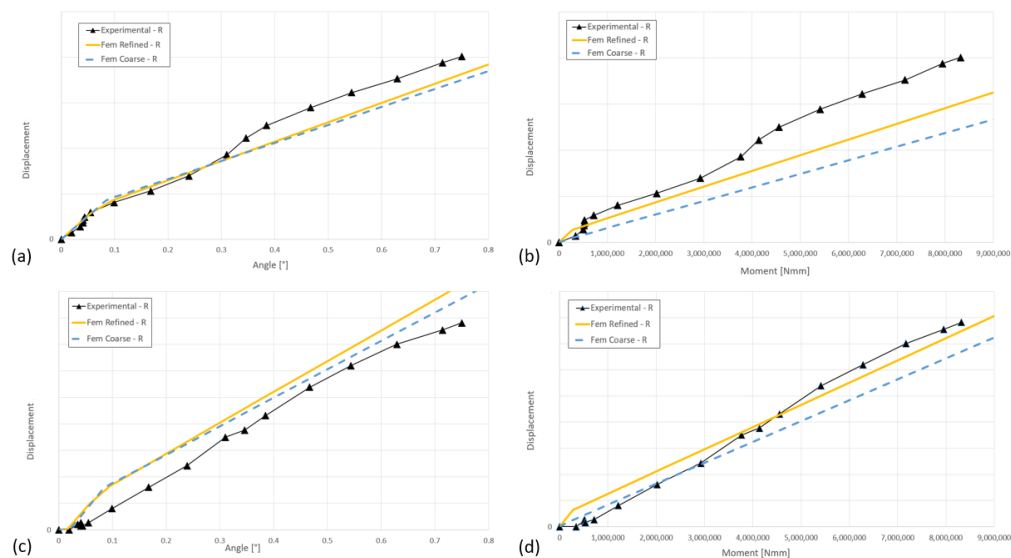


Figure 15. Comparison between experimental and FE displacement in the concentrated bending: (a) Measured at laser position, as a function of the rotation angle; (b) measured at laser position, as a function of the moment; (c) measured at cable position, as a function of the rotation angle; (d) measured at cable position, as a function of the moment.

In Table 6, the values of the most significant measured experimental strain and the corresponding numerical values are listed. The compressive strain value recorded by the SG 1, 3 and 5 is higher (more negative) closer to the region in contact with the contrast structure while the highest strain in tension is instead achieved on the SG 37, which is placed on the joint connecting the second rib (where the contrast structure is placed) with the panel in the most stressed zone of the collector. Also, in this case, the numerical result is in reasonable accordance with the experimental one. The data listed in Table 6 show that the numerical model is very accurate and that it can reproduce not only the global experimental behaviour, as described above, but also the local values of strain, which turns out very similar to the experimental values.

Table 6. Comparison between the experimental strain at the maximum load along with numerical strain for the concentrated bending evaluated for a selected list of strain gauges.

Ext. n.	Experimental $\mu\epsilon$	Numerical $\mu\epsilon$
1	6	7.1
3	−46	−51
5	−231	−311
37	178	221

3.4. Wind Load Test

The last load scenario investigated is the wind load, with the aim to test the trough with a load which generates an effect similar to the wind effect on field. The experimental test consists of applying a series of weights to each rib of the trough when it is rotated at the 90° position. The resulting load is symmetric and is distributed along the entire structure and is hence similar to the effect of a constant wind acting on the front surface of the trough. A CDF analysis has been done on a model of the collector rotated with an angle of approximately 30° (condition in which the force lift is maximum) with a wind velocity of 50 km/h. On the basis of this result, 14 weights (6 for each traverse, 1 for each rib tip), each of them of 30 kg, have been applied in order to reproduce the same maximum moment inside the parabolic trough collector. For this test the collector has been kept fixed in a fully horizontal condition, blocking the stroke of the actuators on both the sides.

In total 14 weights of 30 kg each, resulting in a total applied weight of 420 kg, were connected to the trough by means of robust cables; two weights were connected to the end of every rib of the trough. During the test, the behaviour of the trough both during the load phase (adding weight) (Figure 16a) and unload phase (removing weight) (Figure 16b) was studied; the load sequence followed to add and remove weight from configuration 1 to 7 is shown in Figure 16. The configurations are intended as sequential and cumulative (during loading) and subtractive (during unloading). The measurements were taken with two lasers and cable transducers placed on the trough when rotated of 90°. The cable transducers were connected to the upper ends of the central rib (4th rib), while the lasers have been aimed toward the back beam, Figure 17. One laser measured the displacement at the centre of the back beam (4th rib), and the other measured the displacement of the back beam in a position corresponding to the 6th rib. All the sensors aimed to measure the vertical displacement. Thus, the loads and boundaries applied in the numerical model aim to replicate the experimental set-up in the configuration with the maximum load applied (configuration 4). In particular, the rotation of the trough was fixed on both ends in both steps. The loads were modelled as a concentrated load and applied for each rib in the same position as for the experiments. The loads applied in the FE model are reported in Figure 17.

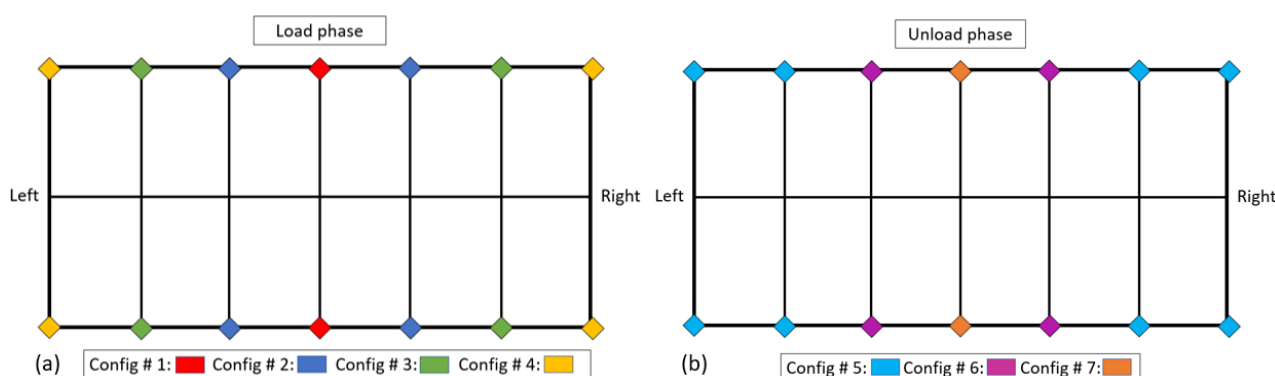


Figure 16. (a) Load phase configurations—(b) unload phase configurations.

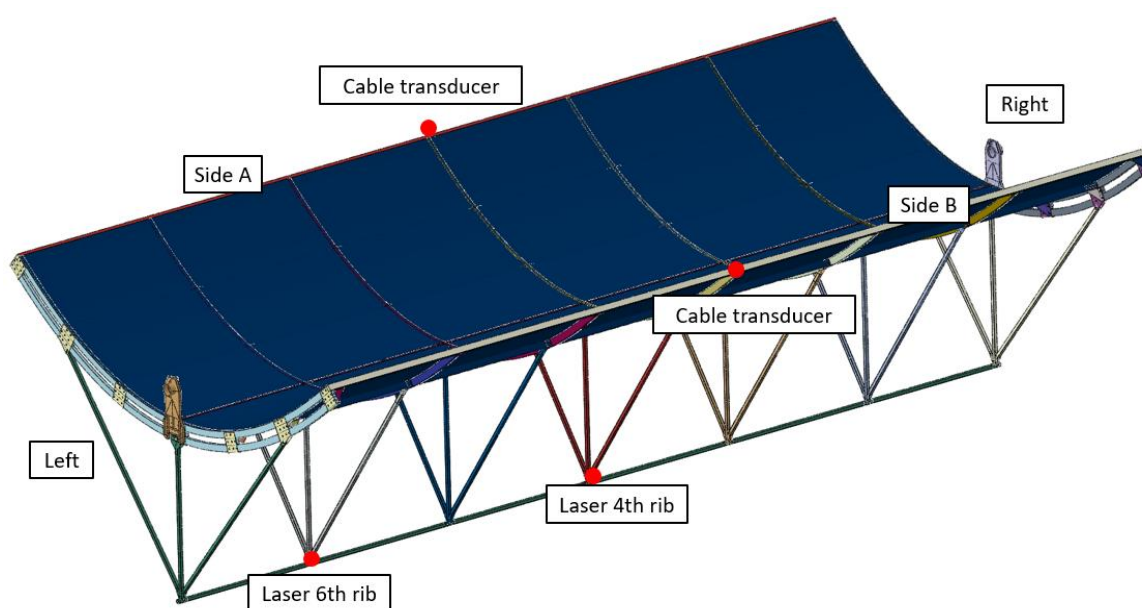


Figure 17. Summary of the measurement instruments and their location for wind load test.

The displacement results are summarized in Table 7. The results have an adequate accuracy especially when considering that the applied load is not very high (only 420 kg) and hence the displacements are very small. Again, the FE model predicts a stiffer trough than the experimental data and the results obtained with the refined mesh are slightly more accurate. On the base of the data, the global validation can be considered achieved.

Table 7. Comparisons between the numerical displacements (coarse and refined) and the experiments for the wind load scenario.

Position	Experimental mm	Fem Coarse mm	Fem Refined mm
Laser 4th rib	−0.512	−0.458	−0.448
Laser 6th rib	−0.330	−0.294	−0.287
Cable Side A	−2.695	−2.674	−2.558
Cable Side B	−2.695	−2.666	−2.566

Once the global validation has been assessed, the local validation of the numerical FE model can be analysed. The numerical values along with the experimental ones are reported in Table 8. The numerical model estimates strain with good accuracy and, considering the SG 1, 3, 5, the symmetric behaviour with respect to the transversal middle plane of

the structure is correctly reproduced by the model. Thus, both the experiments and the FE model have the same symmetry as expected due to the symmetry of the loads and the symmetry of the trough.

Table 8. Experimental strain at the maximum load along with the numerical strain in case of the wind load evaluated for a selected list of strain gauges.

Ext n.	Experimental mε	Numerical mε
1	−53	−49.5
3	−95	−75.1
5	−60	−49.5

4. Increment of the Torsional Stiffness Through a Computer Aided Engineering (CAE) Approach

As reported above in the manuscript, the FE model can be considered as validated and, thus, it can be adopted as a design tool. Therefore, an application which demonstrates the potential of the FE model when used to develop an optimal design solution is reported in this section. The goal is to identify structural modifications which increase the torsional stiffness of the parabolic trough. Indeed, the torsional stiffness is a key aspect of the system because it profoundly affects the optical efficiency of the trough and, in turn, the efficiency of the energy production. However, an increment of the torsional stiffness has to be obtained, while keeping in mind the strict requirement to neither increase the weight substantially nor the cost of the system. The concept consists in increasing the torsional stiffness by adding steel ropes (guy-wires) to the structure. However, it is necessary to determine the most efficient configuration and to quantify the increment of the torsion stiffness in such detail that only the most promising configuration is subsequently experimentally tested.

4.1. Definition of the Most Promising Guy-Wire Configuration

The solution chosen to increase the torsional stiffness is based on adding guy-wires connected with tensioners in order to apply also a desired preload. It must be pointed out that the addition of these stiffeners does not affect the structural integrity of the trough even in case of the failure of one, or all of them. It is also very important to remark that, at the beginning, the procedure is entirely numerical. The numerically tested configurations are reported in Figure 18.

The values of the ratio of the torsional stiffness compared with the reference case (configuration 0, i.e., that without an additional guy-wire), are listed in Table 9.

The analysis of the data listed in Table 9, determines B1 as most promising configuration, which deserves to be experimentally tested. Actually, configuration B1 does not have the highest effect on the torsional stiffness, the most effective configuration being configuration C leading to an increment of the torsional stiffness of 16.31 times, but configuration B1 has the advantage of great simplicity as it is based on only four guy-wires connected to the four vertex of the trough and the centre of the back beam. However, despite its simplicity, an increase of the torsional stiffness of around nine times is expected by means of configuration B1. Furthermore, configuration B1 requires only a few modifications of the actual structure of the trough and it adds a negligible weight to the system and also its application on field appears easy. In the following section, the application of configuration B1 is investigated both from an experimental point of view and by modifying the FE model in order to exactly represent the tested configuration.

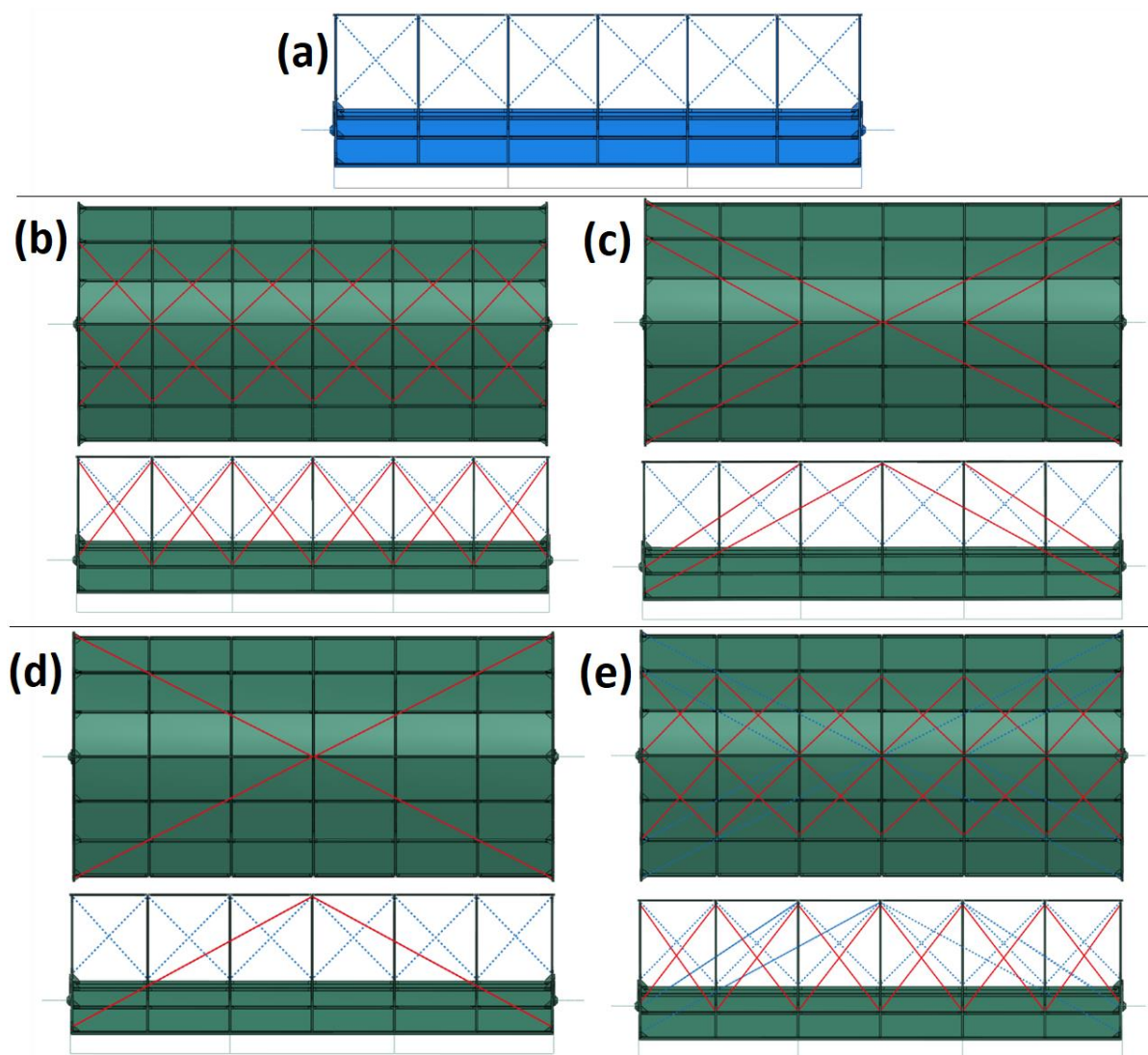


Figure 18. Configuration 0 with the guy-wires adopted in the original set-up (a), configuration A (b), configuration B (c), configuration B1 (d), configuration C (e).

Table 9. Comparison of all the configurations.

	Connector Type	Ratio
Configuration 0—No preload	guy-wire	1.00
Configuration A—No preload	guy-wire	10.17
Configuration B—No preload	guy-wire	10.77
Configuration B1—No preload	guy-wire	8.65
Configuration C—No preload	guy-wire	16.31

4.2. Experimental Test Adopting Guy-Wire Configuration B1—Results

Configuration B1 shown in Figure 18 has been experimentally tested using a differential torsion load case. The structure has to be slightly modified in order to join the four steel wires to the actual trough. The leading idea behind all the activities is to try to reduce any modification of the structure and the additional costs as much as possible. The connection of the steel wires to the structure is shown in Figure 19.

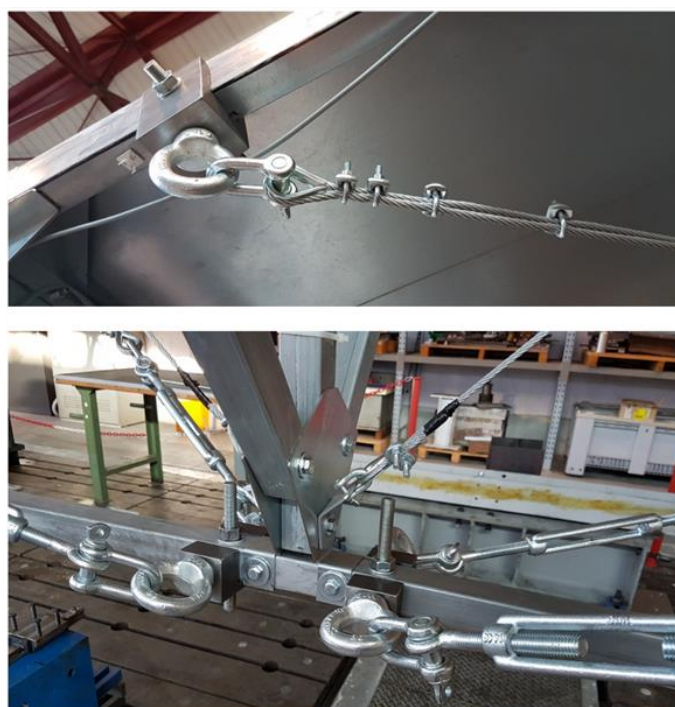


Figure 19. Detail of the connection of the gripping device with the transverse (**top**) and the back beam (**bottom**).

A tensioner is placed on each of the four guy-wires to apply a desired tension preload to the steel wire. The test configuration and the kind of applied load lead to an uneven load of the guy-wires, with the two diagonal wires being more loaded during the application of torsion, while the other two wires, placed on the opposite diagonal, undergo a decrease of their load. The torsional stiffness depends on the stiffness of the guy-wires, but the stiffness of the guy-wires depends in turn on the applied preload. Therefore, it is crucial to be able to measure the initial preload applied to the system. Indeed, a decrease of the preload is expected to result in a corresponding decrease of the torsional stiffness. Thus, the preload has been measured using a tensiometer. The chosen version is a mechanical instrument, which is able to measure the tension applied on a guy-wire by measuring the load needed to bend it in a local three point bending application. It is a DIN8M model produced by Cami s.r.l, with a maximum measurable load of 10 kN and it can be applied to wires of 6 mm to 19 mm diameter. The sensibility of the instrument is 0.2 kN. Due to its working scheme, the tensiometer applies a certain load on the guy-wire and it can therefore potentially not exactly measure the real tension; furthermore, the presence of the instrument itself can potentially affect the measurements. These potential effects are very relevant especially if the wire is short and tend to become negligible when the length is sufficiently long. In the present case, a specific test has been performed to check the perturbation effect of the tensiometer. One guy-wire was grounded on one end, the other was left linked to the trough and an industrial weight scale was connected in series with the wire, as shown in Figure 20b. The test consists of the application of a certain preload using the tensioner and measuring this preload with the weight scale. Then using the tensiometer, Figure 20a, the preload is measured again and any changes to the value of the weight scale are checked. The value read by the tensiometer is very close to the value read by the weigh scale and the distortional effect of the tensiometer is negligible with the length adopted in current test. Therefore, the tensiometer provides reliable and reasonably accurate measurements.

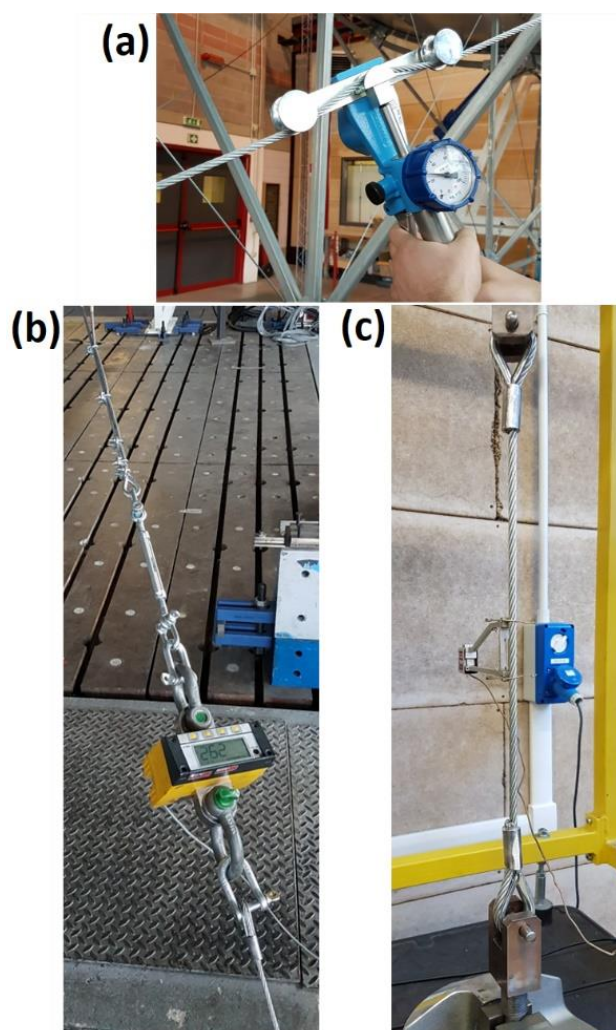


Figure 20. Measurement using the tensiometer (a), set-up for testing the perturbation effect of the tensiometer (b), experimental set-up of the tension test of the guy-wires (c).

The experimental torsional stiffness as a function of the preload is listed in Table 10, showing that the use of the guy-wires in the B1 configuration significantly improves the stiffness of the trough and that, by increasing the preload, the stiffness can be further increased. In particular, adopting a preload of 7.8 kN, the torsional stiffness increases around ten times. The effect of the preload on the torsional stiffness is highlighted in Figure 21 and the effect of the preload on the stiffness clearly tends to decrease after a certain value of the preload. This means that the preload effect is not linear and therefore it is not possible to infinitely increase the stiffness by increasing the preload, but, beyond a certain value, an increase of the preload has almost no further effects on the stiffness.

Table 10. Experimental torsional stiffness as a function of the preload. The ratio is calculated by dividing the torsional stiffness with the torsional stiffness in the case without guy-wires.

Preload (kN)	Ratio
0	1
2.6	5
3.8	6.5
5.8	8.2
7.8	10.2

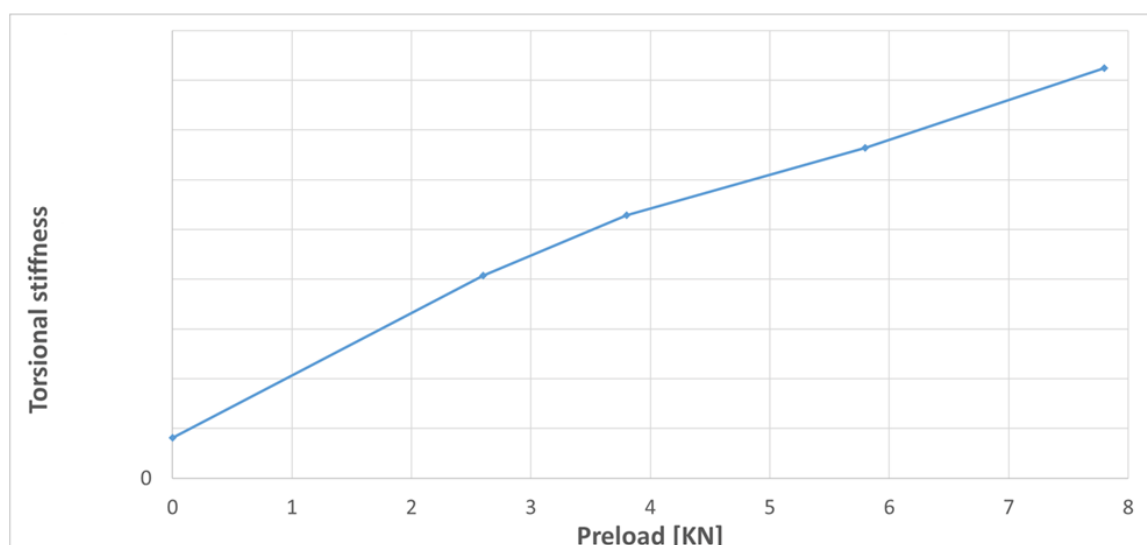


Figure 21. Experimental effect of the preload on the torsional stiffness.

4.3. Experimental Test Adopting Guy-Wire Configuration B1—Discussion

As reported in the results above, it is evident that the response of the wires depends on the preload i.e., the stiffness of the ropes changes according to the applied load. The knowledge of this effect is crucial for a correct numerical representation in the FE model. In order to investigate this effect, an experimental program testing the wires was carried out. A steel wire coupon with a length of 500 mm was tested in a hydraulic MTS machine. An extensometer was connected to the wire in order to measure the real elongation and the applied load was measured by means of a load cell. The tests were performed in displacement control applying a maximum load of 10 kN. The experimental set-up is shown in Figure 20c and the results in terms of load versus elongation (measured by the extensometer) are reported in Figure 22. Four tests on two different specimens (wire 1 and wire 2) were performed and several conclusions can be drawn. First, by loading and unloading the ropes, there is a hysteresis cycle. This phenomenon is an indicator of energy dissipation. The main reason is due to the friction between individual the steel wires composing the entire steel wire. A second important effect is that the response of the first load cycle (0–10 kN) is very different for each of the tested guy-wires (wire 1 and wire 2) while the response of the second cycle is very similar. This means that the ropes require at least one load cycle before they exhibit a stable response. The final conclusion, which is also the most interesting for the present purposes, regards the stiffness. It is evident that the stiffness of the guys changes with the applied tension load. Approximately below 3 kN, the stiffness is low and very non-linear, while the stiffness tends to become linear and constant with a value higher than for lower loads above the 3 kN limit. The reason why the torsional stiffness of the trough depends on the preload is thus verified and explained.

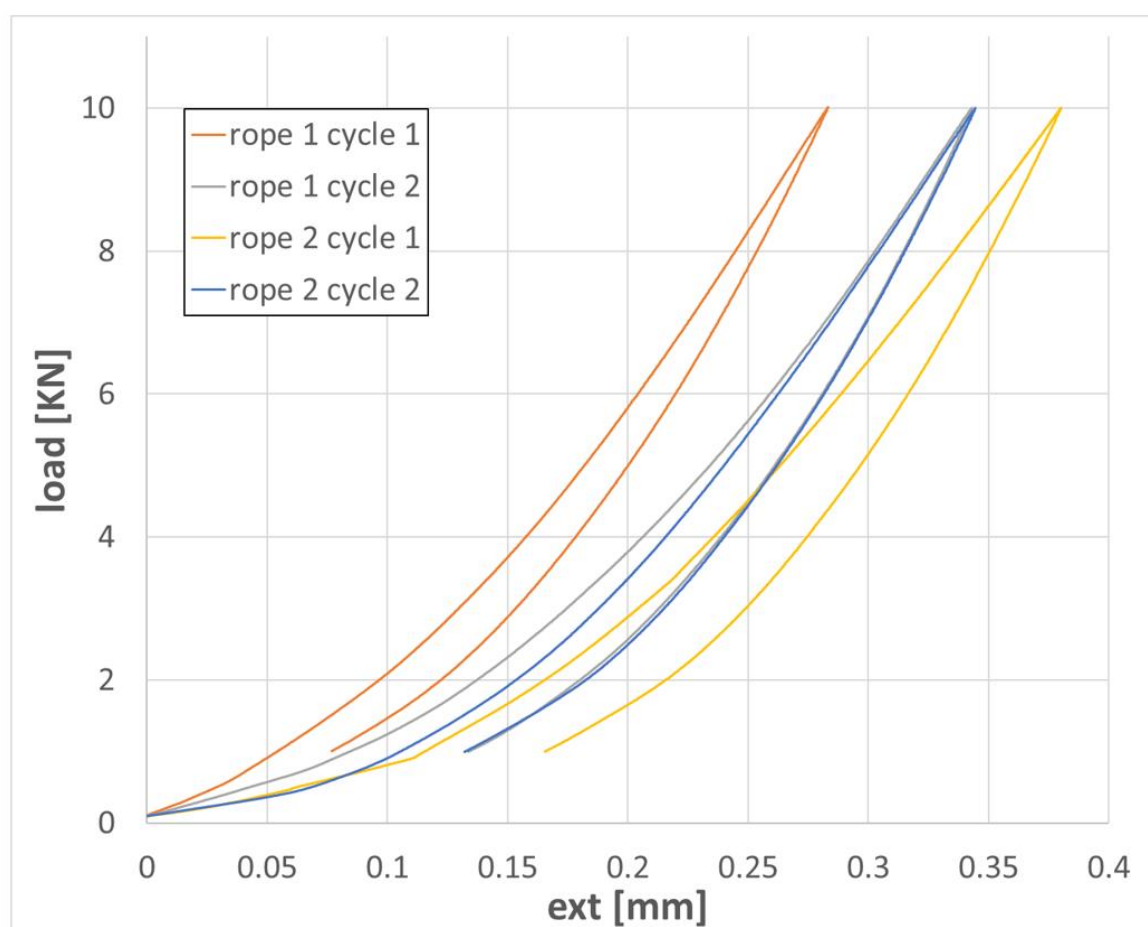


Figure 22. Load versus displacement curves of the tested guy-wires.

4.4. Numerical Model of the Differential Torsion Test with the Guy-Wire Configuration B1

The numerical model described in Section 3 has been updated in order to replicate the real experimental set-up as well as possible. In particular, the grippings have been modelled, and Figure 23 shows an overview of the FE model along with the numerical models of the grippings.

The connection of the guy-wire to the support is obtained by a coupling between the end of the wire and a circular portion of the gripping device. The elements adopted for the gripping are solid with a reduced integration scheme. The guy-wires are modelled as connectors to which a non-linear stiffness can be assigned. The non-linear stiffness of Figure 22 has been implemented. The software ABAQUS does not allow the definition of a different behaviour during the load and the unload of the connectors and, therefore an average stiffness law between the load and the unload curve has been selected. It is worth remembering that the tensile data refers to a 500 mm length specimen and the data has been scaled considering the real length of the rope around 7 m. Finally, it has also been possible in the FE model to apply a desired preload. Results in terms of moment versus rotation between experiments and numerical model are reported in Figure 24. The numerical curves reproduce the experimental curves appropriately especially for the high preload. In case of the lower preload, the discrepancies are higher due to the inaccuracy of the tensiometer. Indeed, the measurement error of the tensiometer is fixed and, therefore, its effect is proportionally higher when the measured load tension is low rather than high.

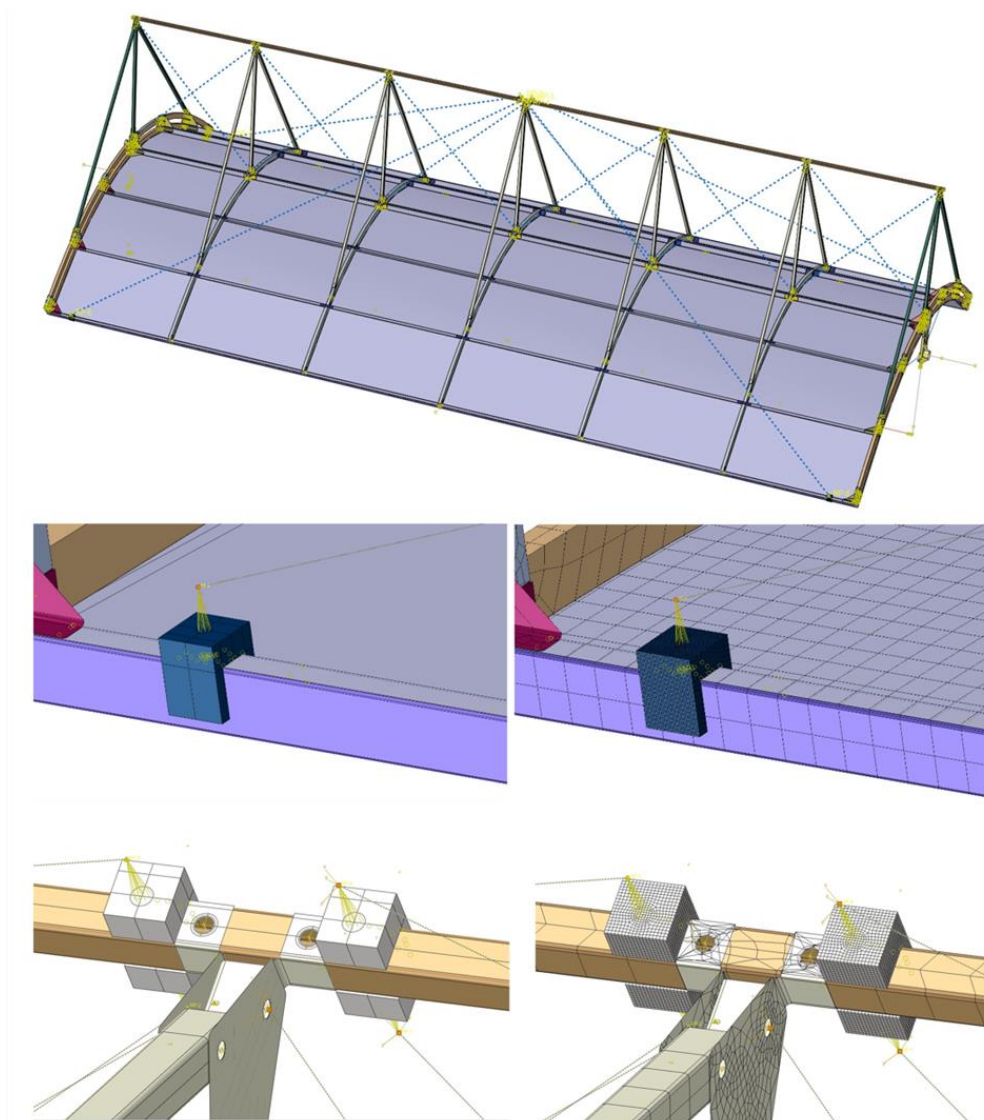


Figure 23. Overview of the FE model with the guy-wire configuration B1 (top), detail of the gripping device applied on the traverse, with the mesh (centre), detail of the gripping device applied on the back beam, with the mesh (bottom).

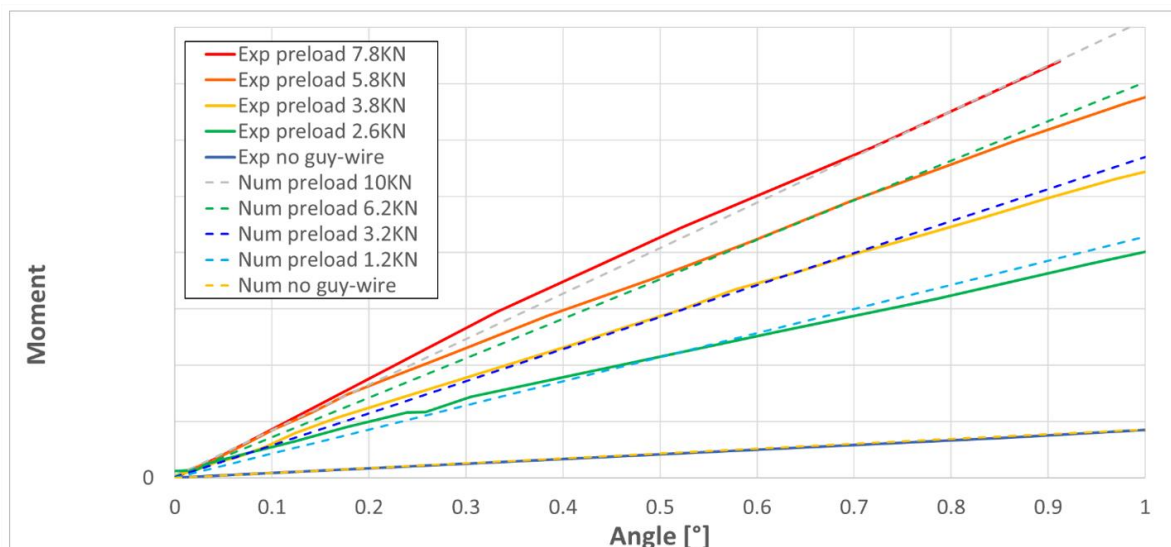


Figure 24. Numerical results of the differential torsion tests compared with the experiments.

5. Conclusions

A FE model of an innovative parabolic trough collector has been built in order to demonstrate the possibility to obtain a reliable tool for the structural investigation of a very complex component such as a parabolic trough. The final model is able not only to reproduce the global behaviour of the collector (displacement, rotation, stiffness) but also its local strain state. This goal is achieved by means of a FE model, which can be run even on a regular workstation without the need of a much more expensive server with higher computational capabilities. Such results can be achieved by means of a proper numerical simulation obtained by a rigorous modelling method. Probably, the most important result of the model is the very accurate estimation of the torsional stiffness, which is one of the most important parameters for the design of the trough, due to its strict relationship with its energetic efficiency (see Table 3). At the same time, also the local behaviour (stress/strain state) is satisfactorily reproduced, adopting the validated model with a refined mesh. Tables 4–6 show satisfactory results, in particular for higher values of strain. On the other hand, very low values seem to be affected by intrinsic noise in the experimental measurements. Thus, local areas (or specific components) of the structure can be analysed with a good accuracy without the creation of sub models. The model has been validated for very different load cases at both local and global level. Thus, it can be considered reliable enough to become a valuable tool for designers who can exploit it to reduce the number of costly experimental tests and to allow an easier evaluation of different and new design updates. The proposed model and the related methodology can further lead to a significant reduction of the design cost of the trough, allowing a better exploitation of the strength of the material (guaranteeing at the same time high reliability). In turn, this leads to a reduction of the global weight, thus helping make the CSP system more feasible economically. Finally, an example of a computer-aided engineering approach is shown, in which various guy-wire configurations are numerically compared and evaluated in order to find the most promising solution to improve the torsional stiffness of the trough. The predicted most promising configuration is then chosen and experimentally tested demonstrating again the very good predictive capability of the FE model and the great potential of the CAE approach. Finally, it is worth mentioning that, even if the validity of the result of the model is limited to the present industrial product, the methodological approach bears wide generality and may thus be used for the analyses of similar products.

Author Contributions: Conceptualization, M.G., L.C., and C.L.; methodology, A.G., L.A., M.F., F.C., A.M., M.G., L.C., S.C., and G.A.G.S.; software, A.G., L.A., M.F., and S.C.; formal analysis, A.G., L.A., M.F., and S.C.; investigation, A.G., L.A., M.F., F.C., A.M., M.G., L.C., C.L., S.C., and G.A.G.S.; writing—original draft preparation, A.G. and S.C.; writing—review and editing, F.C., A.M., L.C., C.L., S.C., and G.A.G.S.; supervision, M.G., L.C., and C.L.; funding acquisition, M.G., L.C., and C.L. All authors have read and agreed to the published version of the manuscript.

Funding: This research was partially funded by ENI S.p.A, in the framework of the agreement with Politecnico di Milano n. 4400007601.

Institutional Review Board Statement: Not applicable.

Informed Consent Statement: Not applicable.

Data Availability Statement: Data sharing not applicable.

Acknowledgments: The parabolic trough collector was designed and constructed at the laboratory of the Politecnico di Milano in 2016 and has been developed by the joint effort of the Politecnico di Milano, Massachusetts Institute of Technology funded by ENI.

Conflicts of Interest: Some employers of the funding entity are included the authors' list. However, methods and results are presented without any influence and/or interpretation of the funding sponsor.

References

1. Barlev, D.; Vidu, R.; Stroeve, P. Innovation in concentrated solar power. *Sol. Energy Mater. Sol. Cells* **2011**, *95*, 2703–2725. [CrossRef]
2. Jebasingh, V.K.; Herbert, G.M. A review of solar parabolic trough collector. *Renew. Sustain. Energy Rev.* **2016**, *54*, 1085–1091. [CrossRef]
3. Kumaresan, G.; Sudhakar, P.; Santosh, R.; Velraj, R. Experimental and numerical studies of thermal performance enhancement in the receiver part of solar parabolic trough collectors. *Renew. Sustain. Energy Rev.* **2017**, *77*, 1363–1374. [CrossRef]
4. Zamparelli, C. Storia, Scienza e Leggenda Degli Specchi Ustori di Archimede. 2005. Available online: <https://www.gses.it/pub/specchi1.pdf> (accessed on 23 January 2017).
5. IRENA. Renewable Power Generation Cost in 2014. 2015. Available online: https://irena.org/-/media/Files/IRENA/Agency/Publication/2015/IRENA_RE_Power_Costs_2014_report.pdf (accessed on 23 January 2017).
6. Geyer, M.; Lüpfer, E. EUROTROUGH—Parabolic Trough Collector Developed for Cost Efficient Solar Power Generation. In Proceedings of the 11th SolarPACES International Symposium on Concentrated Solar Power and Chemical Energy Technologies, Zurich, Switzerland, 4–6 September 2002.
7. Energy.gov | SunShot initiative. Available online: <https://energy.gov/eere/sunshot/sunshot-initiative> (accessed on 23 January 2017).
8. Mokheimer, E.M.; Dabwan, Y.N.; Habib, M.A.; Said, S.A.; Al-Sulaiman, F.A. Techno-economic performance analysis of parabolic trough collector in Dhahran, Saudi Arabia. *Energy Convers. Manag.* **2014**, *86*, 622–633. [CrossRef]
9. Asfar, J.A.; Ayadi, O.; Salaymeh, A.A. Design and Performance Assessment of a Parabolic Trough Collector. *Jordan J. Mech. Ind. Eng.* **2014**, *8*, 1–5.
10. Marcotte, P.; Manning, K. Development of an advanced large-aperture parabolic trough collector. *Energy Procedia* **2013**, *49*, 145–154. [CrossRef]
11. Christian, J.; Ho, C. Finite element modeling and ray tracing of parabolic trough collectors for evaluation of optical intercept factors with gravity loading. In Proceedings of the ASME 2011 5th International Conference on Energy Sustainability & 9th Fuel Cell Science, Engineering and Technology Conference, Washington, DC, USA, 7–10 August 2011.
12. Meiser, S.; Kleine-Büning, C.; Uhlig, R.; Lüpfer, E.; Schiricke, B.; Pitz-Paal, R. Finite Element Modeling of Parabolic Trough Mirror Shape in Different Mirror Angles. In Proceedings of the ESFuelCell2012-91264. ASME. ASME 2012 6th International Conference on Energy Sustainability ESFuelCell2012, San Diego, CA, USA, 23–26 July 2012.
13. Sartori, F.T.; Heimsath, A. FEA study of innovative solutions for parabolic trough collector design. *AIP Conf. Proc.* **2019**, *2126*, 120021. [CrossRef]
14. Gilioli, A.; Abbiati, L.; Fossati, M.; Cadini, F.; Manes, A.; Giglio, M.; Carnelli, L.; Volpato, C.; Cardamone, S. Experimental Investigation on the Mechanical Behavior of an Innovative Parabolic Trough Collector. *Energies* **2019**, *12*, 4438. [CrossRef]
15. Fernández-García, A.; Zarza, E.; Valenzuela, L.; Pérez, M. Parabolic trough solar collectors and their applications. *Renew. Sustain. Energy Rev.* **2010**, *14*, 1695–1721. [CrossRef]
16. Gunther, M.; Joemann, M.; Csambor, S. *Advanced CSP Teaching Materials—Chapter 5: Parabolic Trough Collector*; DLR-deutsches zentrum für luft- und raumfahrt: Cologne, Germany, 2011.
17. Price, H.; Lüpfer, E.; Kearney, D.; Cohen, E.Z.e.G. Advances in Parabolic Trough Solar Power Technology. *J. Sol. Energy Eng.* **2002**, *124*, 109–125. [CrossRef]
18. Cardamone, S. Ottimizzazione Strutturale di un Collettore Solare Parabolico Mediante la Tecnologia dell’incollaggio. Master’s Thesis, Politecnico di Milano, Milano, Italy, 2013.
19. Crescenzo, C.D. Numerical, Experimental and NDT Analyses on Adhesively Bonded Joints of a Parabolic Trough Collector. Master’s Thesis, Politecnico di Milano, Milano, Italy, 2017.
20. Giannuzzi, G.M.; Majorana, C.E.; Miliozzi, A.; Nicolini, V.S.e.D. Structural Design Criteria for Steel Components of Parabolic-Trough Solar Concentrators. *J. Sol. Energy Eng.* **2007**, *129*, 382–390. [CrossRef]
21. Salomoni, V.A.; Majorana, C.E.; Giannuzzi, G.M. *New Trends in Designing Parabolic trough Solar Concentrators and Heat Storage Concrete Systems in Solar Power Plants. Chapter of Solar Energy*; InTechOpen publisher: London, UK, 2010; pp. 268–292. Available online: <https://www.intechopen.com/books/solar-energy/new-trends-in-designing-parabolic-trough-solar-concentrators-and-heat-storage-concrete-systems-in-so> (accessed on 23 January 2017).